Environ Fluid Mech (2016) 16:695–719
DOI 10.1007/s10652-015-9438-8

ORIGINAL ARTICLE

Coupling between free-surface fluctuations, velocity fluctuations and turbulent Reynolds stresses during the upstream propagation of positive surges, bores and compression waves

Xinqian Leng[1] · **Hubert Chanson**[1]

Received: 27 August 2015 / Accepted: 17 November 2015 / Published online: 27 November 2015

Abstract In open channel, canals and rivers, a rapid increase in flow depth will induce a positive surge, also called bore or compression wave. The positive surge is a translating hydraulic jump. Herein new experiments were conducted in a large-size rectangular channel to characterise the unsteady turbulent properties, including the coupling between free-surface and velocity fluctuations. Experiments were repeated 25 times and the data analyses yielded the instantaneous median and instantaneous fluctuations of free-surface elevation, velocities and turbulent Reynolds stresses. The passage of the surge front was associated with large free-surface fluctuations, comparable to those observed in stationary hydraulic jumps, coupled with large instantaneous velocity fluctuations. The bore propagation was associated with large turbulent Reynolds stresses and instantaneous shear stress fluctuations, during the passage of the surge. A broad range of shear stress levels was observed underneath the bore front, with the probability density of the tangential stresses distributed normally and the normal stresses distributed in a skewed single-mode fashion. Maxima in normal and tangential stresses were observed shortly after the passage of a breaking bore roller toe. The maximum Reynolds stresses occurred after the occurrence of the maximum free-surface fluctuations, and this time lag implied some interaction between the free-surface fluctuations and shear stress fluctuations beneath the surge front, and possibly some causal effect.

Keywords Tidal bores · Positive surges · Compression waves · Turbulence · Turbulent Reynolds stresses · Physical modelling

Electronic supplementary material The online version of this article (doi:10.1007/s10652-015-9438-8) contains supplementary material, which is available to authorized users.

✉ Hubert Chanson
h.chanson@uq.edu.au;
http://www.uq.edu.au/~e2hchans/

[1] School of Civil Engineering, The University of Queensland, Brisbane, QLD 4072, Australia

1 Introduction

A tidal bore is a surge of water propagating upstream in an estuarine zone when the tidal flow turns to rising and rushes into a funnel shaped river mouth with shallow waters [1, 2, 3] (Fig. 1). Figure 1 presents photographs of advancing tidal bores. The bore forms typically during the early flood tide when the tidal range exceeds 4–6 m and the estuary

Fig. 1 Tidal bore propagation. **a** Undular bore of the Dordogne River at St Pardon (France) on 20 October 2013 about 18:05—bore propagation from *left* to *right*. **b** Breaking bore of the Qiantang River at Laoyanchang (China) on 11 October 2014 at 14:00—Bore propagation from *left* to *right*. **c** Tidal bore of Qiantang River impacting on the eighteenth century estuary seawall at Xinchang (China) on 11 October 2014 at 12:57

Fig. 1 continued

bathymetry amplifies the tidal range with a low freshwater level [3]. Tidal bores can be dangerous, impacting adversely on man-made structures and endangering lives (Fig. 1c). They can be also a major touristic and sport attraction (Fig. 1a).

In an open channel, more generally, a sudden change in flow: e.g., a sudden closure of a downstream gate, will induce a positive surge, characterised by an increase in flow depth [4, 5, 6]. It is also called compression wave by analogy with compressible flow [7]. After formation, the positive surge may be analogous to a translating hydraulic jump [8, 9]. The shape of the bore front can be characterised by its Froude number Fr_1, whose expression may be derived based upon momentum considerations for an irregular cross-section [10]:

$$Fr_1 = \frac{V_1 + U}{\sqrt{g \times \frac{A_1}{B_1}}} \tag{1}$$

where V_1 is the initial flow velocity positive downstream, U is the bore celerity positive upstream, g is the gravity acceleration, A_1 is the initial flow cross-section area and B_1 is the initial free-surface width.

Considering a positive surge propagating in a prismatic rectangular channel, a dimensional analysis links the instantaneous turbulent flow properties at a position (x, y, z) and at a time t as functions of the positive surge properties, initial flow properties, channel geometry and fluid properties:

$$\frac{d}{d_1}, \frac{V_i}{V_1}, \frac{P}{\rho \times g \times d_1}, \frac{\tau_{ij}}{\rho \times V_1^2}, \ldots = f\left(\frac{x}{d_1}, \frac{y}{d_1}, \frac{z}{d_1}, t \times \sqrt{\frac{g}{d_1}}, \frac{V_1 + U}{\sqrt{g \times d_1}}, \rho \times \frac{(V_1 + U) \times d_1}{\mu}, \frac{W}{d_1}, \theta, \frac{k_s}{d_1}, \frac{g \times \mu^4}{\rho \times \sigma^3}, \ldots\right) \quad (2)$$

where d is the instantaneous water depth, V_i is the instantaneous velocity component i, P is the instantaneous pressure, τ_{ij} is the instantaneous Reynolds stress tensor component, i, j = x, y, z, x is the coordinate in the flow direction, y is the horizontal transverse coordinate measured from the channel centreline, z is the vertical coordinate measured from channel bed, t is the time, U is the surge celerity, d_1 is the initial depth, V_1 is the initial flow velocity, θ is the angle between bed slope ad horizontal, k_s is the equivalent sand roughness height of the channel bed, W is the channel width, g is the gravity acceleration, ρ and μ are the water density and dynamic viscosity respectively, and σ is the surface tension between air and water. In Eq. (2) on the right handside, the fifth and sixth terms are the tidal bore Froude Fr_1 and Reynolds numbers Re respectively, and the tenth term is the Morton number Mo which is a function of fluid properties and gravity constant only.

For the past 25 years, research into unsteady turbulence in positive surges has been active, with fundamental laboratory works in rectangular channels [11, 12, 13, 14] and new computational fluid dynamics modelling [15, 16]. Field studies have been fewer and encompassed the free-surface measurements of Benet and Cunge [17] and Ponsy and Carbonnell [18] in man-made canals, and the turbulence measurements of Kjerfve and Ferreira [19], Chanson et al. [20], Furgerot et al. [21], and Reungoat et al. [22, 23] in tidal bores in natural systems. All studies demonstrated the intense shear stress generated during the bore passage, associated with massive sediment processes in both laboratory and field [24, 25, 26]. Recent field observations indicated that the bore passage induced immediately some bed surface erosion followed by delayed bulk erosion [27, 28]. Despite all these advances, the current knowledge in the basic flow physics remains limited, in particular the coupling between free-surface fluctuations, water turbulence and air bubble entrainment [29, 30].

It is the aim of this contribution to characterise the turbulent properties of bore fronts including the coupling between free-surface and velocity fluctuations. This is based upon a series of laboratory experiments conducted in a large facility to investigate the instantaneous free-surface, velocity and Reynolds stress fluctuations in positive surges. Both breaking bores and undular bores were investigated under controlled flow conditions. Each experiment was repeated 25 times, and both instantaneous median and fluctuating properties were characterised for a relatively broad range of Froude numbers ($1.2 < Fr_1 < 2.2$) and Reynolds numbers ($9 \times 10^4 < Re < 3.5 \times 10^5$). The results are compared and discussed in the context of the upstream propagation of positive surges and tidal bores in an open channel.

2 Experimental facility and instrumentation

New experiments were performed in a 19 m long, 0.7 m wide tilting flume. The flume was made of glass sidewalls and smooth PVC bed. The initially steady flow was supplied by an upstream water tank equipped with baffles and flow straighteners, leading the water to to the flume through a smooth three-dimensional convergent intake. The discharge provided by the tank was measured by a magneto flow meter with an accuracy of 10^{-5} m^3/s. A fast-

closing Tainter gate was located next to the downstream end of the channel at x = 18.1 m, where x is measured from the upstream end of the flume. A radial gate was located further downstream at x = 18.88 m, followed by a free overfall (Fig. 2).

The water depths were measured using pointer gauges with an accuracy of 0.001 m in steady flows. The unsteady water depths were recorded with a series of acoustic displacement meters (ADMs). A Microsonic™ Mic + 35/IU/TC unit was located immediately downstream of the Tainter gate. Nine ADMs Microsonic™ Mic + 25/IU/TC were spaced upstream of the gate between x = 17.81 m and x = 0.96 m. All acoustic displacement meters were placed above the channel centreline, calibrated against pointer gauge measurements in steady flows and they sampled non-intrusively the free-surface at 200 Hz. The applicability of ADM to breaking bores with air bubble entrainment was tested against sidewall dSLR photography. The differences between the two methods were small to negligible.

In steady and unsteady flows, the velocity measurements were conducted with an acoustic Doppler velocimeter (ADV) Nortek™ Vectrino + (Serial No. VNO 0436) equipped with a three-dimensional sidelooking head at a range of vertical elevations z above the invert. The ADV was located at x = 8.5 m on the channel centreline. The velocity range was ± 1.0 m/s, the sampling rate was 200 Hz, and the ADV was setup with a transmit length of 0.3 mm, a sampling volume of 1 mm height and a power setting: High. The post processing of the ADV data was conducted following Chanson [13] and Docherty and Chanson [31]. The steady flow data processing included the removal of communication errors, the removal of average signal to noise ratio data less than 5 dB and the removal of average correlation values less than 60 %; and the phase-space thresholding technique developed by Goring and Nikora [32] and implemented by Wahl [33] was applied. The unsteady flow post-processing was limited to a removal of communication errors, although, for z < 0.030 m, some vertical velocity data might be adversely impacted by the bed proximity. Both the acoustic displacement meters and acoustic Doppler velocimeter were synchronised within ± 1 ms and sampled simultaneously at 200 Hz.

Additional information was obtained with a dSLR camera Pentax™ K-3, video camera Sony™ HDR-XR160E (50fps, resolution: 1920p × 1080p) and digital camera Casio™ Exlim Ex10 (Movie modes: 120fps, resolution: 640p × 480p; 240fps, resolution: 512p × 384p). Further details on the experimental facility and instrumentation were reported in Leng and Chanson [34].

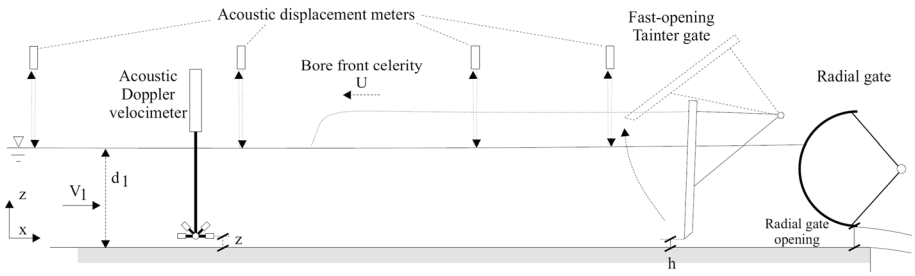

Fig. 2 Definition sketch of the experimental setup with an overview of the flume

2.1 Data accuracy

The error of the pointer gauge data was ±0.5 mm in steady flow, the accuracy on the acoustic displacement meter data was 0.18 mm [35], the error on the velocity components was 1 % of the velocity range (herein ±1 m/s), that is ±0.01 m/s [36].

The repeatability of the experiment was very carefully tested by repeating a number of experiments using different individuals operating the gate, with a gate closure less than 0.2 s for each experiment and on different days. The results showed that the bore front arrival time, bore height, bore celerity… were basically identical. Small differences were observed linked to the fluctuating nature of the bore roller free-surface, as observed in stationary hydraulic jumps and breaking bores [37, 38, 39].

2.2 Experimental flow conditions

This study focused on fully-developed bores (i.e., hydraulic jump in translation) for which the mean properties were independent of time and space, thus independent of the generation process. The ADV sampling location ($x = 8.5$ m) was selected accordingly after preliminary tests. Detailed velocity measurements showed that the initially steady flow was partially developed at $x = 8.5$ m and the dimensionless boundary layer thickness δ_o/d_1 ranged between 0.3 and 0.5 depending upon the initial flow conditions [34].

Four initial discharges ($Q = 0.101$, 0.085, 0.071 and 0.055 m^3/s) were tested (Table 1). For each experiment, the positive surge was generated by the rapid closure of the Tainter gate and the surge propagated upstream as sketched in Fig. 2. The radial gate was fully opened for the breaking bore experiments; it was initially partially closed to raise the initial water depth d_1 during the undular surge experiments. The bulk of experiments were performed with a horizontal slope ($S_o = 0$) (Table 1). A steeper bed slope was used simply to decrease the initial water depth while maintaining the initial flow rate, thus achieving an initially supercritical flow and generating tidal bores with high Froude numbers. The slope was very gentle and barely perceptible compared to the channel length.

Ensemble-average experiments were performed herein. For each run, the instruments were started 60 s prior to gate closure; the sampling stopped when the surge reached the upstream intake structure. A total of 25 runs were repeated for each set of ensemble-average experiments. The median free-surface elevations and velocity components were calculated from the total ensemble, as well as the fluctuating properties. Table 1 summarises the present experimental flow conditions.

3 Basic observations

For a hydraulic jump in translation, basic theoretical considerations demonstrate that the strength of the bore is linked to its Froude number (Eq. 1) [8]. When the Froude number Fr_1 is less than one, the surge cannot form. For a Froude number between 1 and 1.3–1.5, the bore has an undular form: that is, the front is a smooth wave followed by a train of quasi-periodic secondary waves called whelps or undulations [2, 40]. Photographs of undular and breaking bore propagations are presented in the Digital Appendix. In an undular bore, the rate of energy dissipation is small to negligible, and the pressure distributions are not hydrostatic [41, 42]. Field and laboratory data showed a maximum in dimensionless wave amplitude and steepness for $Fr_1 \approx 1.3$–1.4, corresponding to the

Table 1 Experimental flow conditions and types of measurements (present study)

S_o	Q (m^3/s)	Radial gate opening (m)	h (m)	Bore type	d_1	Fr_1	Instrumentation	Type of measurements
0	0.055	N/A	0–0.105	Breaking & undular	0.121–0.172	1.2–1.6	ADM	Instantaneous
	0.071						ADM	Instantaneous
	0.085						ADM	Instantaneous
	0.101						ADM & ADV	Instantaneous & ensemble-average
0	0.055	0.051–0.125	0–0.105	Breaking & undular	0.188–0.196	1.1–1.3	ADM & ADV	Instantaneous & ensemble-average
	0.071						ADM	Instantaneous
	0.085						ADM	Instantaneous
	0.101						ADM & ADV	Instantaneous & ensemble-average
0.0025	0.071	N/A	0–0.105	Breaking & undular	0.113–0.143	1.2–1.6	ADM	Instantaneous
	0.085						ADM	Instantaneous
	0.101						ADM	Instantaneous
0.005	0.055	N/A	0–0.071	Breaking & undular	0.072–0.105	1.6–2.1	ADM & ADV	Instantaneous & ensemble-average
	0.071						ADM	Instantaneous
	0.085						ADM	Instantaneous
	0.101						ADM	Instantaneous
0.0075	0.055	N/A	0–0.071	Breaking	0.063–0.096	1.9–2.3	ADM	Instantaneous
	0.071						ADM	Instantaneous
	0.085						ADM	Instantaneous
	0.101						ADM & ADV	Instantaneous & ensemble-average

Ensemble-averaged experiments were repeated 25 times

d_1 Initial flow depth measured at x = 8.5 m, Fr_1 bore Froude number, h Tainter gate opening after rapid closure, Q water discharge, S_o bed slope

apparition of some slight breaking at the first wave crest [2, 13]. For larger Froude numbers ($Fr_1 > 1.4$–1.6), the bore had a breaking front with a marked roller. In a breaking bore, the roller toe is a flow singularity where vorticity is generated and air is entrapped [11, 29]. Figure 3 shows a high-shutter speed photograph of a roller toe. The roller toe formed a continuous line, herein called the roller toe perimeter. The transverse profile of the roller toe perimeter showed some pseudo-periodic shape, indicating the existence of non-linear structures, streamwise vortices and streaks [39]. Present observations hinted a physical process similar to a plane mixing layer [43].

The generation and upstream propagation of bores was recorded non-intrusively. A typical example is shown in Fig. 4 for a breaking bore, presenting the median free-surface elevation and instantaneous fluctuations at $x = 18.17$ m (i.e., downstream of Tainter gate) and $x = 17.41$ m and 8.5 m (i.e., upstream of Tainter gate). The instantaneous fluctuations were characterised by the difference between third and first quartiles ($d_{75} - d_{25}$), which would be equal to 1.3 times the standard deviation of the total ensemble for a Gaussian distribution. The ensemble-averaged free-surface data highlighted the abrupt increase in water level associated with the passage of a breaking bore roller (Fig. 4), and a significant upward free-surface curvature followed by a secondary wave motion with an undular bore (data not shown). For all the experimental conditions (Table 1), the data indicated a sharp increase in free-surface fluctuations with the propagation of a positive surge, although the propagation of a breaking bore was typically associated with higher maximum free-surface fluctuations than that of a an undular bore. In each case the free-surface fluctuations showed a marked maximum $(d_{75} - d_{25})_{max}$ shortly after the passage of the bore, and the corresponding time delay Δt will be further discussed below.

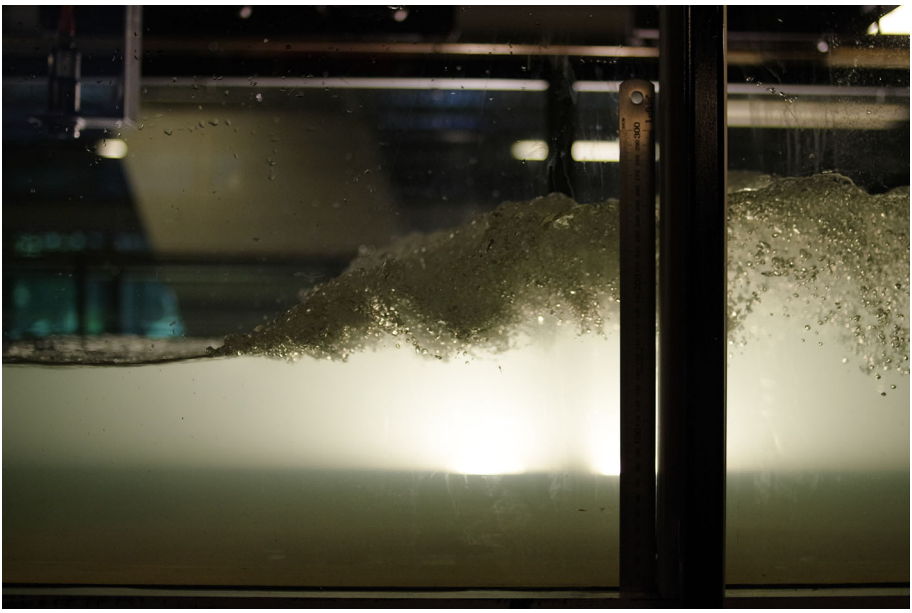

Fig. 3 Upstream propagation of a breaking bore—breaking bore propagation from right to left; Flow conditions: $Q = 0.101$ m^3/s, $S_o = 0.0025$, Radial gate opening = fully-opened, $h = 0$ m, $Fr_1 = 2$

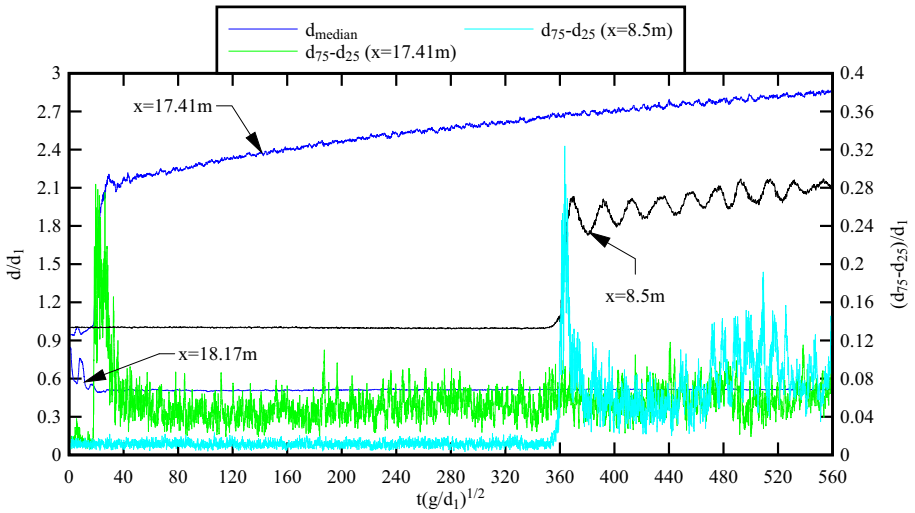

Fig. 4 Ensemble-averaged time variations of the median free-surface elevations and free-surface fluctuations at different longitudinal locations for a breaking bore: Q = 0.055 m^3/s, $Fr_1 = 1.5$

For breaking bores, the maximum free-surface fluctuations $(d_{75} - d_{25})_{max}$ recorded at x = 8.5 m are presented in Fig. 5 as functions of the Froude number. The data are compared to earlier breaking bore data, stationary hydraulic jump data and stationary hydraulic jump calculations. Despite differences in instrumentation reported in the caption of Fig. 5, all the data showed the same trend: namely, the maximum free-surface fluctuations increased with increasing Froude number (Fig. 5). The data were best correlated by:

$$\frac{(d_{75} - d_{25})_{max}}{d_1} = 0.331 \times (Fr_1 - 1)^{0.63} \quad \text{Positive surges } (1.38 < Fr_1 < 2.2) \qquad (3)$$

$$\frac{\eta'_{max}}{d_1} = 0.172 \times (Fr_1 - 1)^{0.94} \quad \text{Stationary hydraulic jumps } (1.9 < Fr_1 < 8.5) \qquad (4)$$

where η'_{max} is the maximum free-surface elevation standard deviation in a stationary hydraulic jump. Both Eqs. (3) and (4) are compared to the data in Fig. 5.

4 Velocity measurements

4.1 Presentation

Instantaneous velocity measurements were conducted at x = 8.5 m (Table 1). Herein V_x is positive downstream, V_y is positive towards the left sidewall and V_z is positive upwards. Both breaking and undular bores were investigated. For breaking bores, all data showed a sharp rise in water level associated with an abrupt decrease in longitudinal velocity at the arrival of the roller and passage of the roller toe. The transverse velocity showed some large fluctuations around zero during the roller passage. The vertical velocity component showed an initial acceleration, which was more significant at higher vertical elevations,

Instrumentation	Positive surges/bores	Stationary hydraulic jump
Photographic/video observations	LENG and CHANSON (2015a)	MISRA et al. (2006)
Wave gauges	--	MADSEN (1981), MOUAZE et al. (2005), MURZYN et al. (2007)
Acoustic displacement meters	DOCHERTY and CHANSON (2012), CHANSON and TOI (2015), Present study	KUCUKALI and CHANSON (2008), MURZYN and CHANSON (2009), CHACHEREAU and CHANSON (2011), WANG et al. (2014), WANG and CHANSON (2015)

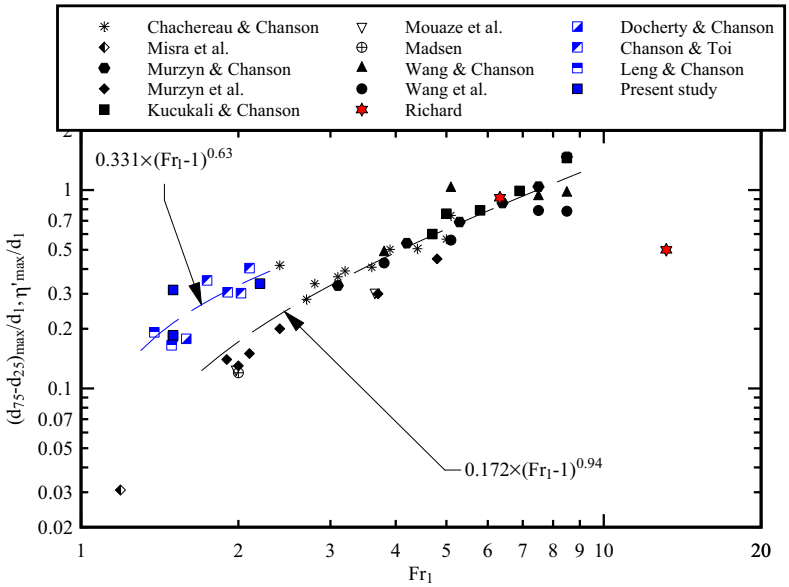

Fig. 5 Maximum instantaneous free-surface fluctuations $(d_{75} - d_{25})_{max}$ at x = 8.5 m as functions of the Froude number Fr_1—comparison with positive surge data (*blue symbols*), stationary hydraulic jump data (*black symbols*), stationary hydraulic jump theoretical calculations (Richard 2013) (*red symbols*) and correlations (*dashed lines*)

particularly close to the free-surface. In undular bores, the longitudinal velocity decelerated following the passage of the first wave crest and then oscillated about a mean value in a quasi-periodic manner. The period of longitudinal velocity component oscillation corresponded to the free-surface undulation period, but the oscillations in longitudinal velocity were out of phase in comparison to the undulation of the free-surface. The transverse and vertical velocity data also showed quasi-periodic oscillations following the undulations of the free-surface. Next to the free-surface, the data indicated a marked increase in vertical velocity magnitudes, consistent with boundary conditions set by the free-surface elevation undulations.

Since the propagation of tidal bores was a highly turbulent and unsteady process, a series of ensemble-averaged velocity measurements were conducted at x = 8.5 m and the results yielded the instantaneous median velocity and velocity fluctuations defined as the difference between third and first quartiles of velocity data ($V_{75} - V_{25}$) for the longitudinal, transverse and vertical components. Figure 6 shows a typical data set, with the ensemble-averaged median water depth at the velocity sampling location highlighted by the black solid line. In Fig. 6, t = 0 corresponded to the Tainter gate

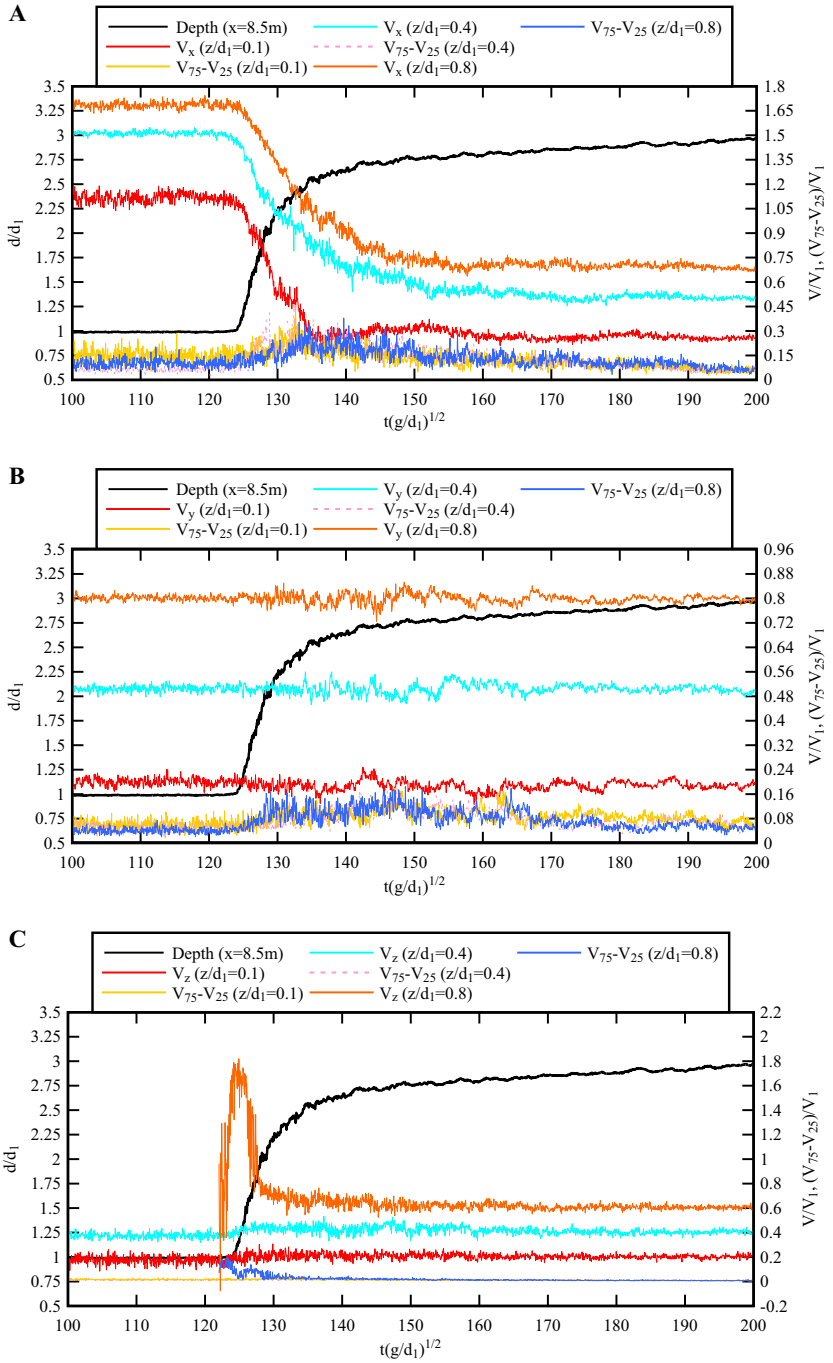

Fig. 6 Time-variations of instantaneous ensemble-averaged velocity components and velocity fluctuations ($V_{75} - V_{25}$) at different vertical elevations z/d_1 for a breaking bore—flow conditions: $Q = 0.101$ m^3/s, $Fr_1 = 2.2$, $x = 8.5$ m, velocity data offset by $+0.2$ for all elevations. **a** Longitudinal velocity component V_x. **b** Transverse velocity component V_y. **c** Vertical velocity component V_z

closure, and the velocity data were offset vertically by +0.2 for all elevations in each graph.

Within the investigated flow conditions, all data showed a marked deceleration of the longitudinal velocity component V_x during the bore passage as seen in Fig. 6a. This was associated with an initial acceleration followed by deceleration of the vertical velocity component V_z at all elevations, regardless of the bore type. After the passage of a breaking bore, the longitudinal velocity (after the deceleration phase) was almost constant with some fluctuations (Fig. 6a). Breaking bores were further associated with a transient recirculation next to the bed, after the rapid deceleration. This unsteady flow feature indicated a transient flow reversal immediately after the passage of the bore and was previously reported in laboratory and in the field [13, 44]. The mean value of the transverse velocity V_y was zero in the initial steady flow.

During the passage of a breaking bore, the transverse velocity showed large fluctuations around zero, before becoming almost nil with small fluctuations after the complete passage of the roller region. The vertical velocity showed a sharp increase as the free-surface rose up, before some deceleration at the inflection point of the free-surface curvature. This pattern was most significant at the higher vertical elevation close to the free-surface and it was directly linked to the streamline and free-surface curvature ahead of the roller. With the passage of an undular bore, the longitudinal, transverse and vertical velocity components showed a quasi-periodic oscillatory pattern associated with the propagation of the first wave crest and secondary undulations. The maximum velocity amplitude tended to occur simultaneously with the free-surface troughs, implying some out-of-phase oscillation [45, 13].

4.2 Velocity fluctuations

The turbulent velocity fluctuation data showed a drastic increase in fluctuations for all three velocity components at all elevations associated with the passage of a positive surge. At the lowest vertical elevation ($z/d_1 = 0.1$), larger velocity fluctuations tended to be observed. The vertical velocity fluctuations were overall greater than the other two components for the same flow condition, most remarkably in the upper water column ($z/d_1 = 0.8$). In breaking bores, marked peaks in the three velocity component fluctuations $(V_{x,75} - V_{x,25})_{max}$, $(V_{y,75} - V_{y,25})_{max}$ and $(V_{z,75} - V_{z,25})_{max}$, occurred slightly after the passage of the bore roller (Fig. 7a) whereas, in undular bores, local maxima appeared repetitively following the train of undulations (data not shown). The maximum velocity fluctuations $(V_{x,75} - V_{x,25})_{max}$, $(V_{y,75} - V_{y,25})_{max}$ and $(V_{z,75} - V_{z,25})_{max}$ in a breaking bore with Froude number $Fr_1 = 1.5$ are presented as functions of the vertical elevation in Fig. 7b1. The corresponding time lag Δt_V between the maximum fluctuation and the bore arrival time is shown in Fig. 7b2 as a function of the vertical elevation. The time lag Δt_V was consistently larger than the time lag Δt for maximum free-surface fluctuations. The results indicated that the vertical velocity component was typically associated with the largest magnitude in maximum velocity fluctuations, and most significant difference in peak fluctuations between the lower and upper water column, the largest velocity fluctuations being recorded in the upper water column. On the other hand, the maximum longitudinal velocity fluctuations were larger next to the bed. All velocity components showed some increase in time lag Δt_V with increasing distance from the bed. Within the experimental flow conditions listed in Table 1, breaking bores at higher Froude numbers

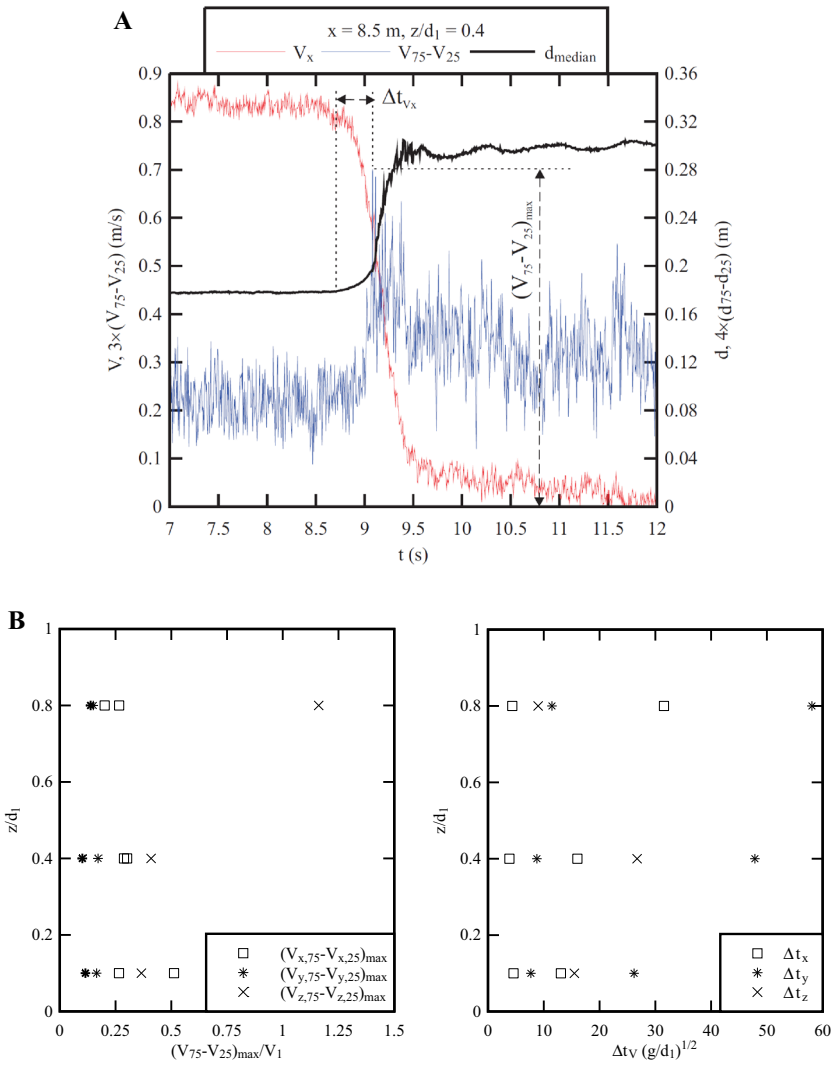

Fig. 7 Maximum velocity fluctuation $(V_{75} - V_{25})_{max}$ during the passage of the bore and corresponding time lag Δt_V between the maximum velocity fluctuations and the arrival of the bore front. **a** Annoted graph of time-variations of instantaneous ensemble-averaged longitudinal velocity and velocity fluctuations $(V_{75} - V_{25})$: $Fr_1 = 1.5$, $z/d_1 = 0.4$, $Q = 0.101$ m^3/s, $x = 8.5$ m. **b** Vertical distributions of maximum velocity fluctuation $(V_{75} - V_{25})_{max}$ after the passage of the bore and time lag Δt_V between the maximum velocity fluctuations and the arrival of the bore front for $Fr_1 = 1.5$, $x = 8.5$ m. (**b1**, *Left*) Maximum velocity fluctuation $(V_{75} - V_{25})_{max}$.(**b2**, *Right*) Time lag Δt_V

tended to have higher peak fluctuations than undular bores and even breaking bores with lower Froude numbers. Lastly the upper water column was associated with a broader scatter of time lag in comparison to the mid and lower water column.

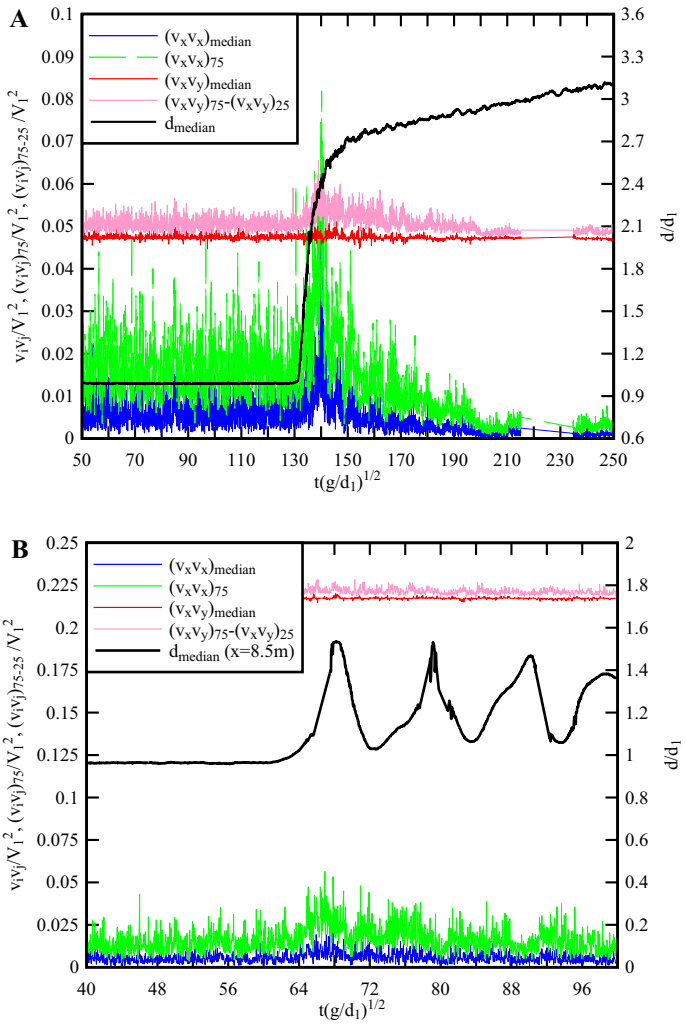

Fig. 8 Time variations of water depth ad turbulent Reynolds stresses during a positive surge: median turbulent stress and fluctuation data. **a** Breaking bore: $Q = 0.101$ m^3/s, $Fr_1 = 2.2$, $z/d_1 = 0.1$, $x = 8.5$ m—tangential stresses and difference between third and first quartiles of tangential stresses were offset by $+0.1$ m^2/s^2. **b** Undular bore: $Q = 0.101$ m^3/s, $Fr_1 = 1.2$, $z/d_1 = 0.1$, $x = 8.5$ m—tangential stresses and difference between the third and first quartiles of the tangential stresses were offset by $+0.1$ m^2/s^2

5 Turbulent reynolds stresses

5.1 Presentation

The Reynolds stress tensor characterises the transport resulting from the turbulent motion induced by velocity fluctuations with a subsequent increase of momentum exchange: $\tau_{ij} = \rho \times v_i \times v_j$ where the velocity fluctuation v_i is the deviation between the measured velocity and the ensemble-average [46]:

$$v_i = V_i - \overline{V_i} \quad (5)$$

where V_i is the instantaneous velocity component measurement, $\overline{V_i}$ is the instantaneous ensemble-median value and i, j = x, y z. Herein both normal and tangential Reynolds stresses were calculated based upon the ensemble-averaged velocity data [47]. Figure 8 shows typical time variations of instantaneous ensemble-averaged Reynolds stresses and Reynolds stress fluctuations. In Fig. 8, the data were collected near the bed at $z/d_1 = 0.1$. In each graph, the solid black line denoted the ensemble-median free-surface variations.

All the data indicated that the propagation of a breaking bore was associated with significant increase in both normal and tangential Reynolds stress amplitudes for all vertical elevations within the experimental flow conditions. Maximum stresses were seen in terms of both normal and tangential stress tensor components shortly after the passage of the roller toe. The third quartiles (e.g., $(v_x v_x)_{75}$) and the quartile differences (e.g., $(v_x v_y)_{75} - (v_x v_y)_{25}$) were large beneath the bore front as seen in Figs. 8a and 9. The third quartile is a characteristic large value, while the quartile difference represent a characteristic fluctuation. Both third quartile and quartile difference data exhibited distinctive peaks which were in phase with the stress maxima for the corresponding stresses. The stress amplitudes and stress quartiles appeared to be larger in the upper water column, possibly associated with the highly-fluctuating free-surface and the air–water interactions in the breaking roller.

In undular bores, the Reynolds stress data showed overall a similar trend to that of a breaking bores, but with less pronounced peaks in terms of the normal stress tensors $v_y v_y$ and $v_z v_z$. The magnitudes of both stresses and stress quartiles were lower in undular bores compared to breaking bores for the same discharge. Further the normal stress tensors $v_x v_x$

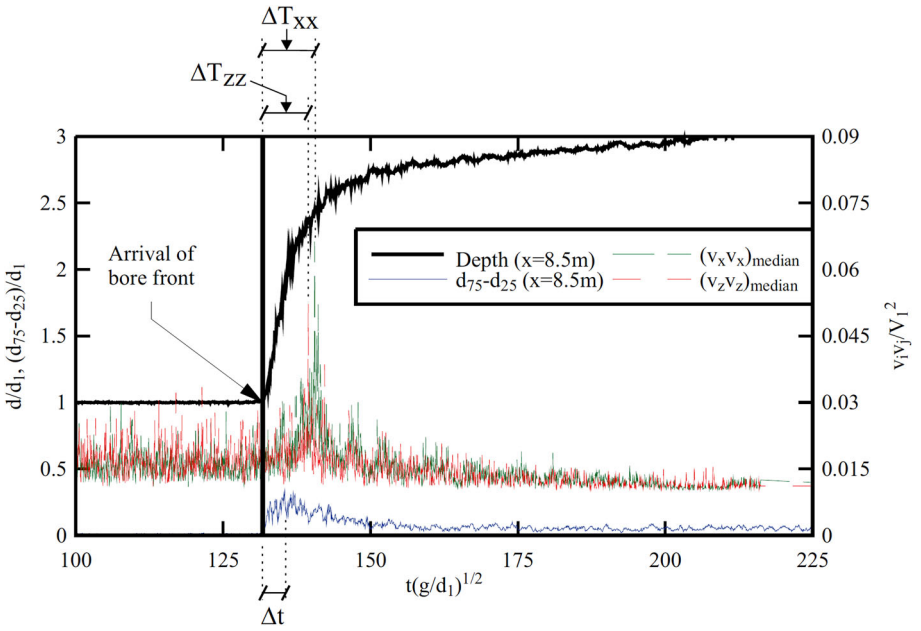

Fig. 9 Comparison between the time of occurrence of the maximum median Reynolds stresses and the time of occurrence of the maximum free-surface fluctuation—flow conditions: $Q = 0.101$ m^3/s, $Fr_1 = 2.2$, $z/d_1 = 0.1$, x = 8.5 m, breaking bore

and $v_z v_z$ showed fluctuations associated with the passage of the bore front and as well as the secondary undulations. The third stress quartile and stress quartile differences data also fluctuated consistently with the corresponding stress tensor components beneath the secondary wave motion. At higher vertical elevations close to the free-surface, the normal stress tensor $v_z v_z$ showed a large increase in stress magnitude and third quartiles compared to data at elevations close to the bed.

5.2 Delayed maximum shear stresses

In the present data, the maximum Reynolds stresses were observed after the bore toe passage as illustrated in Fig. 9. This time lag ΔT was systematically observed. The maximum ensemble-averaged Reynolds stresses $(v_i v_j)_{max}$ associated with the propagation of a positive surge and their time of occurrence ΔT relative to the bore passage were analysed and reported in Appendix 1. Herein the arrival time of the bore front was defined as the instance at which the water level at the velocity sampling point started to rise. Figure 9 provides an example, with the vertical straight black line highlighting the bore arrival time. The first peaks in normal stresses $(v_x v_x)_{median}$ and $(v_z v_z)_{median}$ were seen shortly after this arrival time (Fig. 9) and corresponded to the instance when the first derivative of the free-surface elevation with respect to time started to be non-zero. But the main peak in median shear stresses was always delayed after the bore arrival as seen in Fig. 9.

The results showed large magnitudes of maximum normal stresses next to the channel bed, especially in terms of $v_x v_x$ and $v_z v_z$, in both breaking and undular bores for all experimental conditions (Appendix 1). The time lag ΔT between the maximum normal stress $(v_x v_x)_{max}$ and the arrival of bore front increased with increasing vertical elevation. On the other hand, the normal stress $v_z v_z$ showed a marked increase in maximum stress level with increasing vertical elevation towards the free-surface, whereas the time lag ΔT between $(v_z v_z)_{max}$ and the arrival of bore front decreased with increasing vertical elevation, most significantly in breaking bores. The normal stress $v_y v_y$ was overall smaller than the other normal stress components for the same flow conditions. The undular tidal bores were typically associated with smaller magnitudes in maximum Reynolds stresses for all components, but for $v_z v_z$. In Appendix 1, data with no obvious stress maxima are marked by N/A.

The time lag ΔT between the maximum Reynolds stresses and the arrival of the bore front was compared to Δt, the time lag between the arrival of the bore front and the occurrence of the maximum free-surface fluctuation. Overall, for the same flow condition and vertical elevation, the Reynolds stress tensors in all directions exhibited peak stress levels slightly after the time when the maximum free-surface fluctuation occurred: i.e., $\Delta T > \Delta t$. Figure 9 presents a typical example for a comparison between the two time lags ΔT and Δt. For all flow conditions and all Reynolds stress components, the ratio $\Delta T/\Delta t$ ranged from 0.45 to 6.18, with a mean value of 2.2. The data are regrouped in Fig. 10a, where the ratio $\Delta T/\Delta t$ is plotted as a function of the bore Froude number for tensor stress components. Altogether the median data were best correlated by:

$$\frac{\Delta T}{\Delta t} = 2.2 \times (Fr_1 - 0.73) \quad \text{for } 1.2 < \text{Fr}_1 < 2.2 \tag{6}$$

Equation (6) is compared with the experimental data in Fig. 10a. For comparison, the time lag ΔT for maximum Reynolds stresses was found to be comparable to the time lag Δt_V for maximum velocity fluctuations, within the investigated flow conditions

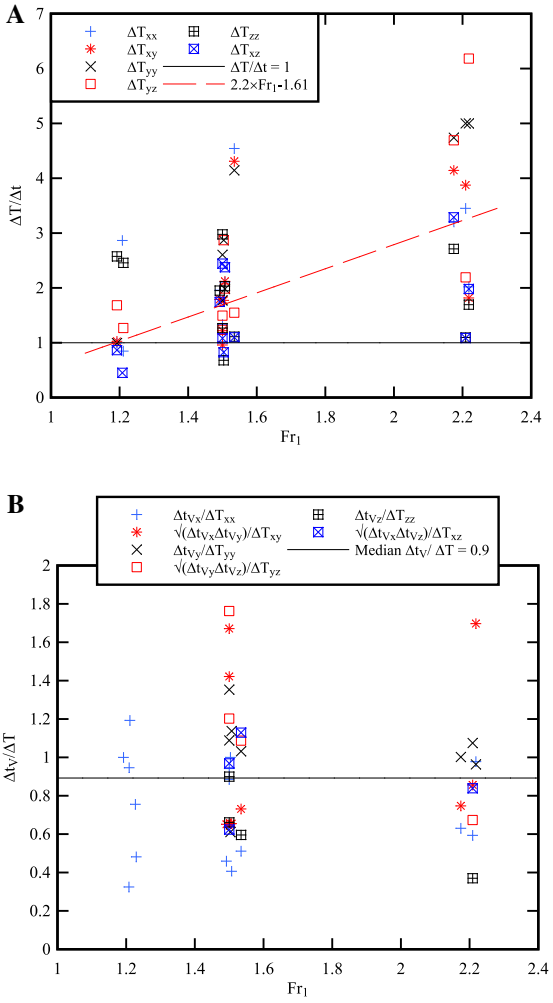

Fig. 10 Comparison between time lags for maximum free-surface fluctuations Δt, maximum velocity fluctuations Δt_V and maximum Reynolds stresses ΔT in positive surges—all ensemble-average data including undular and breaking bores. **a** Ratio $\Delta T/\Delta t$ between the delay in time of maximum Reynolds stresses ΔT and the delay in time of maximum free-surface fluctuations Δt—comparison with Eq. (6). **b** Ratio $\Delta t_V/\Delta T$ between the delay in time of maximum velocity fluctuations Δt_V and the delay in time of maximum Reynolds stresses ΔT

(Table 1). Present data suggested that the maximum Reynolds stresses occurred slightly after the occurrence of maximum velocity fluctuations. On average, the ratio $\Delta t_V/\Delta T$ was typically

$$\frac{\Delta t_V}{\Delta T} \approx 0.9 \quad \text{for } 1.2 < \text{Fr}_1 < 2.2 \tag{7}$$

with most data within 0.6–1.2, as shown in Fig. 10b.

The present results indicated that the maximum Reynolds stresses commonly occurred after the maximum free-surface fluctuations, and that the increase in Reynolds stress might be linked to and caused by the large free-surface fluctuations associated with the bore passage. It is hypothesised that the free-surface fluctuations combined with the longitudinal pressure gradient during the bore front passage, and the turbulent shear in breaking roller to drive the turbulent mixing.

5.3 Probability distribution functions

The probability density functions of instantaneous Reynolds stress data were analysed over a small time span (within 3 s) during, before and after the bore passage for selected flow conditions. The time span selected during the bore passage started immediately before the free-surface rise and ended shortly after the maximum free-surface elevation was reached. Figure 11 presents typical results for normalised probability distribution functions (PDFs) of normal and tangential stresses; the data are presented in a dimensional form. In each figure, the caption and legend provide information on flow conditions and time span; each data point represents the probability of cross-product $v_i \times v_j$ in 0.01 m^2/s^2 intervals. For example, the probability of shear stress from 0.01 to 0.02 m^2/s^2 is represented by the data point labelled 0.01.

Within the experimental flow conditions (Table 1), all normal Reynolds stress tensors exhibited the same PDF shape. That is, the turbulent stress PDFs were skewed to the left with a single mode, with a preponderance of small shear stress amplitude relative to the mean (Fig. 11a), in a manner consistent with field data [23]. The tangential stress data presented a single-mode bell-shaped PDF distribution, with mean value typically about zero (Fig. 11c). For the three selected time spans, the normal Reynolds stresses v_i^2 exhibited a mode between 0 and 0.05 m^2/s^2, corresponding to median shear stresses from 0 to 50 Pa, assuming the water density of 998.2 kg/m^3. Large normal stresses were however observed in excess of 1 m^2/s^2 before, during and after the bore passage, corresponding to shear stresses up to more than 100 Pa. The tangential stresses $v_i v_j$ were mostly distributed between -0.05 and 0.05 m^2/s^2. Note that the magnitude of the maximum normal stresses was two times greater than that of the tangential stresses.

Within the range of experimental conditions, the propagation of positive surges was associated with high turbulent stresses which had large potential in shearing and mixing particles. The bore passage was associated with a highest probability of large normal and tangential stress magnitudes, compared to periods before and after the bore passage. During the period immediately after the surge passage, the data showed comparatively smaller probability of large stress magnitudes (>50 Pa) in terms of both normal and tangential stresses.

6 Discussion

In a natural system, flowing waters have the ability to scour the channel bed, to carry particles heavier than water and to deposit materials. This process of sediment motion is of great economical importance, for example to predict the risks of scouring of bridges and river banks, and to predict the possible bed form changes of riverine and estuarine channels. Traditionally, sediment transport is correlated to the

boundary shear stress [48, 49]. For example, the well-known Shields diagram gives a critical shear stress for sediment motion of 0.1–0.5 Pa for fine sand particles [5, 50]. In channels with cohesive sediments, field observations suggested a critical shear stress for sediment erosion between 0.1 and 10 Pa [51, 52]. Note that existing correlations between sediment entrainment/erosion and shear stress are typically based upon a mean boundary shear stress (e.g., [48, 49, 53, 54, 55]. The present results indicated that the instantaneous shear stresses beneath a positive surge spanned over more than one order of magnitude.

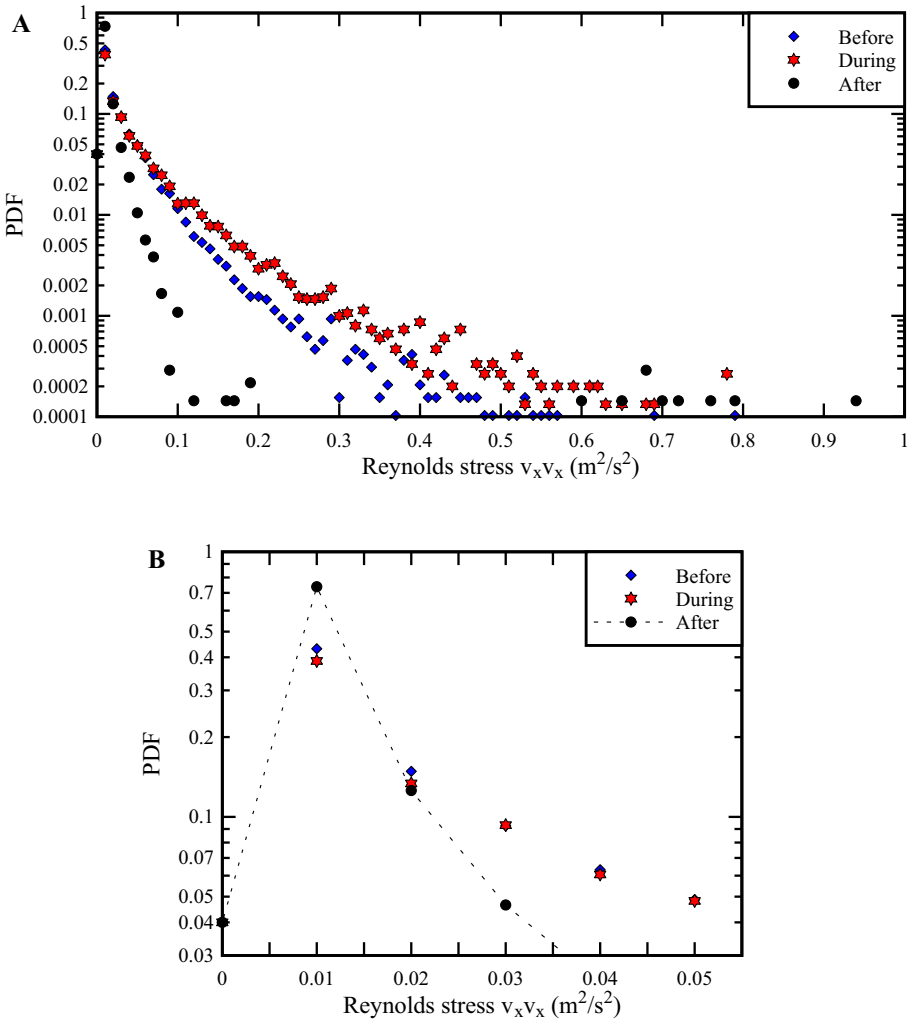

Fig. 11 Probability density functions of turbulent Reynolds stress tensor before, during and after a breaking bore passage—flow conditions Q = 0.101 m^3/s, Fr_1 = 2.2, z/d_1 = 0.1, x = 8.5 m, breaking bore, about 15,000 points per data set—*vertical axes* in logarithmic scale. **a** Normal Reynolds stress tensors v_xv_x: full data set. **b** Normal Reynolds stress tensors v_xv_x: detailed histograms. **c** Tangential Reynolds stress tensor v_xv_y: full data set. **d** Tangential Reynolds stress tensor v_xv_y: detailed histograms

Thus the notion of mean shear stress might not be the most relevant parameter to predict sediment erosion in tidal bore affected estuaries. Indeed the measured instantaneous stress levels were one to two orders of magnitude larger than the critical threshold for sediment motion of cohesive and non-cohesive materials. Present findings suggested that the bore propagation can scour a mobile bed. Once the fluid shear stress exceeds the local strength of the bed, surface erosion occurs initially, in the form of stripping and aggregate fragmentation [56], followed by further mass erosion [57, 58]. The erosion pattern was

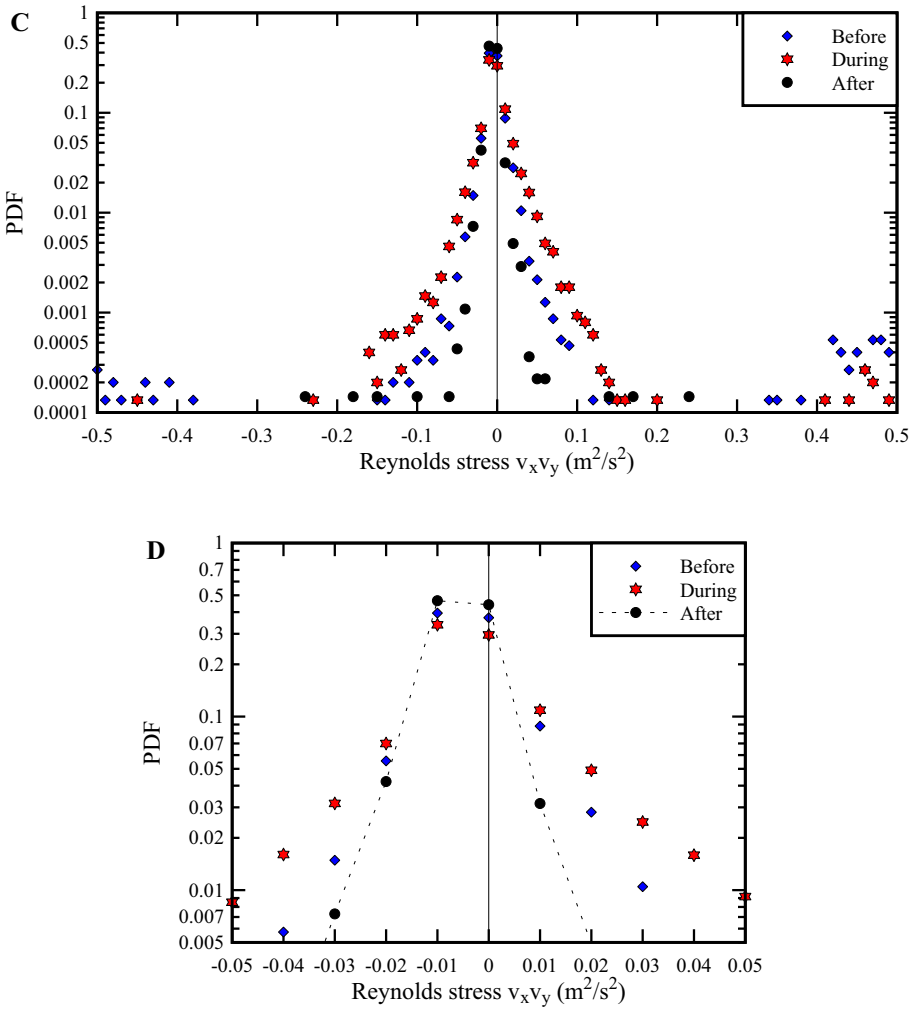

Fig. 11 continued

observed in the field [20, 28] and would be consistent with the observations of large instantaneous shear stresses.

Large instantaneous shear stresses may be associated with turbulent events [59, 60], typically linked to coherent turbulent structures such as eddies and bursting [61, 62]. They are likely to play a major role in terms of sediment scour, transport and accretion as well as contaminant mixing and dispersion [48, 63]. In positive surges, the turbulent event analysis might be considered as an alternative approach to provide details into the turbulent bursts that are responsible for major mixing and sedimentary processes [23]. Classical burst event analyses might however need to be refined specifically for the highly-unsteady rapidly varied flow motion.

7 Conclusion

In an open channel, the propagation of positives surges, bores and compression waves is characterised by intense turbulent mixing associated with high turbulent stress levels. Herein new experiments were conducted in a large-size rectangular channel with a smooth bed to characterise the turbulent properties of bore fronts including the coupling between free-surface and velocity fluctuations. The experiments were repeated 25 times and the data were ensemble-averaged, yielding the instantaneous median and instantaneous fluctuations of free-surface elevation, velocities and turbulent Reynolds stresses. A key feature of the study was the high level of spatial and temporal resolution under carefully-controlled conditions, enabling a fine characterisation of the coupling between free-surface and turbulent shear stress fluctuation during the bore passage. This was ever achieved to date, although the information is critical for future conceptual models and CFD modelling validation.

The passage of the surge front was associated with large free-surface fluctuations, with maximum free-surface fluctuation occurring slightly after the arrival of the front. The free-surface fluctuations were comparable to those recorded in stationary hydraulic jumps for a similar Froude number. Similarly large instantaneous velocity fluctuations were observed for the three velocity components at all elevations. In turn, the propagation of tidal bores was associated with large turbulent Reynolds stresses and instantaneous shear stress fluctuations, particularly beneath the bore front. A broad range of shear stress levels was observed, with the probability density of the tangential stresses distributed normally and the normal stresses distributed in a skewed single-mode fashion. With undular bores, large Reynolds stresses were observed beneath the secondary wave train, lasting longer than during a breaking bore.

Maxima in normal and tangential stresses were observed shortly after the passage of a breaking bore roller toe. The maximum Reynolds stresses occurred after the occurrence of the maximum free-surface fluctuations. The time lag implied some interaction between the free-surface fluctuations and shear stress fluctuations beneath the surge front, and possibly some causal effect. It is hypothesised that the increase in turbulent stresses is caused by the large free-surface fluctuations during the bore front propagation. The rapid fluctuations in roller toe characteristics and roller shape forces a strongly three-dimensional turbulent flow motion, with intense turbulent shear. Simply the propagation of surges and bores is a very complicated turbulent process.

Acknowledgments The authors thank Dr Carlo Gualtieri (University of Napoli "Federico II", Italy), and Professor Shin-ichi Aoki (Osaka University, Japan) for their valuable comments. They also thank Professor Pierre Lubin (University of Bordeaux, France) for his contribution. The authors acknowledge the technical assistance of Jason Van Der Gevel and Stewart Matthews (The University of Queensland). The financial support through the Australian Research Council (Grant DP120100481) is acknowledged.

Appendix 1. Maximum reynolds stresses and corresponding time lag Δt in positive surges

During the present study, the maximum Reynolds stresses and associated time lag ΔT between the occurrences of the maximum stress and bore front arrival were carefully documented. The experimental results are reported below.

S_o	Q (m^3/s)	d_1 (m)	Fr_1	z/d_1	Bore type	$(v_x v_x)_{max}$ (m^2/s^2)	Time lag ΔT_{xx} (s)	$(v_x v_y)_{max}$ (m^2/s^2)	Time lag ΔT_{xy} (s)	$(v_y v_y)_{max}$ (m^2/s^2)	Time lag ΔT_{yy} (s)	$(v_y v_z)_{max}$ (m^2/s^2)	Time lag ΔT_{yz} (s)	$(v_z v_z)_{max}$ (m^2/s^2)	Time lag ΔT_{zz} (s)	$(v_x v_z)_{max}$ (m^2/s^2)	Time lag ΔT_{xz} (s)
0.0075	0.102	0.099	2.2	0.1	Breaking	0.095	1.05	0.039	0.945	0.017	2.60	0.005	*3.215*	0.057	0.88	0.073	1.03
0.0075	0.102	0.099	2.2	0.4	Breaking	0.074	1.665	0.033	*2.155*	0.023	2.465	−0.011	2.44	0.052	1.41	−0.017	1.71
0.0075	0.102	0.1	2.2	0.8	Breaking	0.077	1.795	0.012	*2.015*	0.019	2.6	−0.021	1.14	0.543	0.57	0.05	0.565
0.0005	0.055	0.074	1.5	0.1	Breaking	0.038	1.21	0.007	1.13	0.009	2.09	−0.007	1.46	0.039	1.50	−0.004	1.28
0.0005	0.055	0.074	1.5	0.4	Breaking	0.026	1.57	0.004	1.44	0.006	3.07	−0.006	1.76	0.024	*3.51*	−0.011	*2.88*
0.0005	0.055	0.074	1.5	0.8	Breaking	0.017	***5.36***	0.023	***5.09***	0.004	***4.89***	−0.01	1.83	0.297	1.31	0.027	1.30
0	0.101	0.175	1.5	0.1	Breaking	0.011	1.33	−0.001	1.22	N/A	N/A	N/A	N/A	0.013	1.33	−0.006	1.19
0	0.102	0.181	1.5	0.4	Breaking	0.016	0.52	−0.001	1.21	0.003	1.95	−0.004	1.95	0.011	0.46	−0.005	0.56
0	0.102	0.175	1.5	0.8	Breaking	0.008	1.43	0.001	1.44	0.003	1.35	0.002	1.35	0.015	1.38	−0.005	1.62
0	0.102	0.205	1.2	0.1	Undular	0.009	1.025	0.001	1.065	N/A	N/A	N/A	N/A	0.015	1.51	−0.005	0.64
0	0.102	0.204	1.2	0.4	Undular	0.006	1.495	−0.001	0.35	N/A	N/A	N/A	N/A	N/A	N/A	0.002	1.48
0	0.102	0.203	1.2	0.8	Undular	0.006	0.88	−0.001	0.865	N/A	N/A	−0.001	1.42	0.028	1.82	−0.003	1.19
0	0.056	0.196	1.2	0.1	Undular	0.007	*2.665*	N/A	N/A	N/A	N/A	N/A	N/A	N/A	N/A	−0.003	0.42
0	0.056	0.197	1.2	0.4	Undular	0.006	0.79	N/A	N/A	N/A	N/A	−0.002	1.18	0.103	2.285	N/A	N/A
0	0.056	0.198	1.2	0.8	Undular	0.007	0.925	−0.001	0.955	0.0008	0.925	−0.002	1.565	0.033	2.395	−0.003	0.805

Italic data unusual although likely meaningful data; ***Bold Italic data*** suspicious data

References

1. Tricker RAR (1965) Bores, breakers, waves and wakes. American Elsevier Publ. Co., New York
2. Peregrine DH (1966) Calculations of the development of an undular bore. J Fluid Mech 25:321–330
3. Chanson H (2011) Tidal bores, aegir, eagre, mascaret, pororoca: theory and observations. World Scientific, Singapore. ISBN 9789814335416
4. Henderson FM (1966) Open channel flow. MacMillan Company, New York
5. Chanson H (2004) The hydraulics of open channel flow: an introduction, 2nd edn. Butterworth-Heinemann, Oxford
6. Montes JS (1998) Hydraulics of open channel flow. ASCE Press, New-York
7. Bryson AE (1969) Film notes for waves in fluids. National Committee in Fluid Mechanics Films, No. 21611
8. Lighthill J (1978) Waves in fluids. Cambridge University Press, Cambridge
9. Rayleigh L (1908) Note on tidal bores. Proc R Soc Lond Ser A 81(541):448–449
10. Chanson H (2012) Momentum considerations in hydraulic jumps and bores. J Irrig Drain Eng (ASCE) 138(4):382–385. doi:10.1061/(ASCE)IR.1943-4774.0000409
11. Hornung HG, Willert C, Turner S (1995) The flow field downsteam of a hydraulic jump. J Fluid Mech 287:299–316
12. Koch C, Chanson H (2009) Turbulence measurements in positive surges and bores. J Hydraul Res (IAHR) 47(1):29–40. doi:10.3826/jhr.2009.2954
13. Chanson H (2010) Unsteady turbulence in tidal bores: the effects of bed roughness. J Waterw Port Coast Ocean Eng (ASCE) 136. ISSN 0733-950X)
14. Chanson H (2011) Turbulent shear stresses in hydraulic jumps and decelerating surges: an experimental study. Earth Surf Process Landf 36(2):180–189. doi:10.1002/esp.2031) **(2 videos)**
15. Furuyama S, Chanson H (2010) A numerical solution of a tidal bore flow. Coast Eng J 52(3):215–234. doi:10.1142/S057856341000218X
16. Lubin P, Chanson H, Glockner S (2010) Large eddy simulation of turbulence generated by a weak breaking tidal bore. Environ Fluid Mech 10(5):587–602. doi:10.1007/s10652-009-9165-0
17. Benet F, Cunge JA (1971) Analysis of experiments on secondary undulations caused by surge waves in trapezoidal channels. J Hydraul Res IAHR 9(1):11–33
18. Ponsy J, Carbonnell M (1966) Etude Photogrammétrique d'Intumescences dans le Canal de l'Usine d'Oraison (Basses-Alpes) (Photogrammetric study of positive surges in the oraison powerplant canal). Jl Soc Française de Photogram 22:18–28
19. Kjerfve B, Ferreira HO (1993) Tidal bores: first ever measurements. J Braz Assoc Adv Sci (Ciência e Cultura) 45(2):135–138
20. Chanson H, Reungoat D, Simon B, Lubin P (2011) High-frequency turbulence and suspended sediment concentration measurements in the Garonne River tidal bore. Estuar Coast Shelf Sci 95(2–3):298–306. doi:10.1016/j.ecss.2011.09.012
21. Furgerot L, Mouaze D, Tessier B, Perez L, Haquin S (2013) Suspended sediment concentration in relation to the passage of a tidal bore (sée River Estuary, Mont Saint Michel, NW France). In: Proceedings of the Coastal Dynamics 2013, Arcachon, France, 24–28 June, pp. 671–682
22. Reungoat D, Chanson H, Caplain B (2014) Sediment processes and flow reversal in the undular tidal bore of the Garonne River (France). Environ Fluid Mech 14(3):591–616. doi:10.1007/s10652-013-9319-y
23. Reungoat D, Chanson H, Keevil CE (2015) Field measurements of unsteady turbulence in a tidal bore: the Garonne River in october 2013. J Hydraul Res (IAHR) 53(3):291–301. doi:10.1080/00221686.2015.1021717
24. Greb SF, Archer AW (2007) Soft-Sediment Deformation Produced by Tides in a Meizoseismic Area, Turnagain Arm, Alaska. Geology 35(5):435–438
25. Khezri N, Chanson H (2012) Inception of bed load motion beneath a bore. Geomorphology 153–154:39–47. doi:10.1016/j.geomorph.2012.02.006) **(2 video movies)**
26. Khezri N, Chanson H (2015) Turbulent velocity, sediment motion and particle trajectories under breaking tidal bores: simultaneous physical measurements. Environ Fluid Mech 15(3):633–651. doi:10.1007/s10652-014-9358-z. doi:10.1007/s10652-014-9360
27. Faas RW (1995) Rheological constraints on fine sediment distribution and behavior: The Cornwallis Estuary, Novia Scotia. In: Proceedings of the Canadian Coastal. Conference, Dartmouth, Nova Scotia, pp 301–314
28. Keevil CE, Chanson H, Reungoat D (2015) Fluid flow and sediment entrainment in the Garonne River Bore and tidal bore collision. Earth Surf Process Landf 40(12):1574–1586. doi:10.1002/esp.3735

29. Brocchini M, Peregrine DH (2001) The dynamics of strong turbulence at free surfaces. Part 2. Free-surface boundary conditions. J Fluid Mech 449:255–290
30. Leng X, Chanson H (2015) Turbulent advances of a breaking bore: preliminary physical experiments. Exp Thermal Fluid Sci 62:70–77. doi:10.1016/j.expthermflusci.2014.12.002
31. Docherty NJ, Chanson H (2012) Physical modelling of unsteady turbulence in breaking tidal bores. J Hydraul Eng (ASCE) 138(5):412–419. doi:10.1061/(ASCE)HY.1943-7900.0000542
32. Goring DG, Nikora VI (2002) Despiking acoustic Doppler velocimeter data. J Hydraul Eng (ASCE) 128(1):117–126 **(Discussion: Vol. 129, No. 6, pp. 484–489)**
33. Wahl TL (2003) Despiking acoustic doppler velocimeter data. J Hydraul Eng (ASCE) 129(6):484–487 **(Discussion)**
34. Leng X, Chanson H (2015) Unsteady turbulence during the upstream propagation of undular and breaking tidal bores: an experimental investigation. Hydraulic Model Report No. CH98/15, School of Civil Engineering, The University of Queensland, Brisbane, Australia, 4 video movies. ISBN 978 1 74272 135 4
35. Microsonic (2004) Instruction manual mic+ ultrasonic sensors with one analogue output. Microsonic GmbH, Germany
36. Nortek (2009) Vectrino velocimeter user guide. Nortek AS, Rud
37. Mouaze D, Murzyn F, Chaplin JR (2005) Free surface length scale estimation in hydraulic jumps. J Fluids Eng Trans ASME 127:1191–1193
38. Murzyn F, Mouaze D, Chaplin JR (2007) Air-water interface dynamic and free surface features in hydraulic jumps. J Hydraul Res (IAHR) 45(5):679–685
39. Leng X, Chanson H (2015) Breaking Bore: physical observations of roller characteristics. Mech Res Commun 65:24–29. doi:10.1016/j.mechrescom.2015.02.008
40. Treske A (1994) Undular bores (favre-waves) in open channels—experimental studies. J Hydraul Res (IAHR) 32(3):355–370 **(Discussion: Vol. 33, No. 3, pp. 274–278)**
41. Lemoine R (1948) Sur les Ondes Positives de Translation dans les Canaux et sur le Ressaut Ondulé de Faible Amplitude (On the positive surges in channels and on the undular jumps of low wave height) *Jl La Houille Blanche* 183–185 **(in French)**
42. Montes JS, Chanson H (1998) Characteristics of undular hydraulic jumps. results and calculations. J Hydraul Eng (ASCE) 124(2):192–205
43. Bernal LP, Roshko A (1986) Streamwise vortex structure in plane mixing layers. J Fluid Mech 170:499–525
44. Chanson H, Toi YH (2015) Physical modelling of breaking tidal bores: comparison with prototype data. J Hydraul Res (IAHR) 53(2):264–273. doi:10.1080/00221686.2014.989458
45. Koch C, Chanson H (2008) Turbulent mixing beneath an undular bore front. J Coast Res 24(4):999–1007. doi:10.2112/06-0688.1
46. Bradshaw P (1971) An introduction to turbulence and its measurement. Pergamon Press, Oxford, UK, The Commonwealth and International Library of Science and Technology Engineering and Liberal Studies, Thermodynamics and Fluid Mechanics Division
47. Chanson H, Docherty NJ (2012) Turbulent velocity measurements in open channel bores. Eur J Mech B/Fluids 32:52–58. doi:10.1016/j.euromechflu.2011.10.001
48. Nielsen P (1992) Coastal bottom boundary layers and sediment transport. Advanced series on ocean eng., vol. 4. World Scientific Publication, Singapore
49. van Rijn LC (1993) Principles of sediment transport in rivers, estuaries and coastal seas. Aqua Publ, Amsterdam
50. Graf WH (1971) Hydraulics of sediment transport. McGraw-Hill, New York
51. Sanchez M, Levacher D (2008) Erosion d'une vase de l'estuaire de la Loire sous l'action du courant (Erosion of a mud from the Loire estuary by a flow). Bull Eng Geol Environ 67:597–605. doi:10.1007/s10064-008-0159-9 **(in French)**
52. Jacobs W, le Hir P, van Kesteren W, Cann P (2011) Erosion threshold of sand–mud mixtures. Cont Shelf Res 31(Supplement):S14–S25. doi:10.1016/j.csr.2010.05.012
53. Shields A (1936) Anwendung der Aehnlichkeitsmechanik und der Turbulenz Forschung auf die Geschiebebewegung. *Mitt. der Preussische Versuchanstalt für Wasserbau und Schiffbau*, Berlin, Germany, No. 26
54. Garcia M, Parker G (1991) Entrainment of bed sediment into suspension. J Hydraul Eng (ASCE) 117(4):414–435
55. Garcia M, Parker G (1993) Experiments of the entrainment of sediment into suspension by a dense bottom current. J Geophys Res Oceans 98(C3):4793–4807
56. Pouv KS, Besq A, Gullou SS, Toorman EA (2014) On cohesive sediment erosion: a first experimental study of the local processes using transparent model materials. Adv Water Resour 72:71–83

57. Amos CL, Daborn GR, Christian HA, Atkinson A, Robertson A (1992) In situ erosion measurements on fine grained sediments from the Bay of Fundy. Mar Geol 108:175–196. doi:10.1016/0025-3227(92)90171-D
58. Winterwerp JC, Van Kesteren WGM (2004) Introduction to the physics of cohesive sediment in the marine environment. In: Van Loon T (ed.) Developments in sedimentology, vol. 56. Elsevier, Amsterdam
59. Narasimha R, Rudrakumar S, Prabhu A, Kailas SV (2007) Turbulent flux events in a nearly neutral atmospheric boundary layer. Philos Trans R Soc Ser A 365:841–858. doi:10.1098/rsta.2006.1949
60. Trevethan M, Chanson H (2010) Turbulence and turbulent flux events in a small estuary. Environ Fluid Mech 10(3):345–368. doi:10.1007/s10652-009-9134-7
61. Rao KN, Narasimha R, Narayanan AAB (1971) The "bursting" phenomena in a turbulent boundary layer. J Fluid Mech 48(2):339–352. doi:10.1017/S0022112071001605
62. Nakagawa H, Nezu I (1981) Structure of space–time correlations of bursting phenomena in an open channel flow. J Fluid Mech 104:1–43. doi:10.1017/S0022112081002796
63. Nezu I, Nakagawa H (1993) Turbulence in open-channel flows. IAHR Monograph, IAHR FluidMechanics Section, Balkema Publication, Rotterdam
64. Chachereau Y, Chanson H (2011) Free-surface fluctuations and turbulence in hydraulic jumps. Exp Thermal Fluid Sci 35(6):896–909. doi:10.1016/j.expthermflusci.2011.01.009
65. Kucukali S, Chanson H (2008) Turbulence measurements in hydraulic jumps with partially-developed inflow conditions. Exp Thermal Fluid Sci 33(1):41–53. doi:10.1016/j.expthermflusci.2008.06.012
66. Madsen PA (1981) A model for a turbulent bore. Ph.D. thesis, Technical University of Denmark, Institute of Hydrodynamics and Hydraulic Engineering, Copenhagen, Denmark (also Series Paper No. 28, Technical University of Denmark, Institute of Hydrodyamics and Hydraulic Engineering, Copenhagen, Denmark)
67. Misra SK, Thomas M, Kambhamettu C, Kirby JT, Veron F, Brocchini M (2006) Estimation of complex air-water interfaces from particle image velocimetry images. Exp Fluids 40:764–775. doi:10.1007/s00348-006-0113-1
68. Murzyn F, Chanson H (2009) Free-surface fluctuations in hydraulic jumps: experimental observations. Exp Thermal Fluid Sci 33(7):1055–1064. doi:10.1016/j.expthermflusci.2009.06.003
69. Wang H, Chanson H (2015) Experimental study of turbulent fluctuations in hydraulic jumps. J Hydraul Eng (ASCE) 141(7), Paper 04015010, 10. doi:10.1061/(ASCE)HY.1943-7900.0001010
70. Wang H, Murzyn F, Chanson H (2014) Total pressure fluctuations and two-phase flow turbulence in hydraulic jumps. Exp Fluids 55(11), Paper 1847, 16. doi:10.1007/s00348-014-1847-9